High Entropy and Low Symmetry: Triclinic High-Entropy Molybdates

David Stenzel, Ibrahim Issac, Kai Wang, Raheleh Azmi, Ruby Singh, Jaehoon Jeong, Saleem Najib, Subramshu S. Bhattacharya, Horst Hahn, Torsten Brezesinski, Simon Schweidler,* and Ben Breitung*

ABSTRACT: Metal molybdates constitute a promising class of materials with a wide application range. Here, we report, to our knowledge for the first time, on the preparation and character ization of medium entropy and high entropy metal molybdates, synthesized by an oxalate based coprecipitation approach. The high entropy molybdate crystallizes in a triclinic structure, thus rendering it as high entropy material with the lowest symmetry reported so far. This is noteworthy because high entropy materials usually tend to crystallize into highly symmetrical structures. It is expected that application of the high entropy concept to metal molybdates alters the material's characteristics and adds the features of high entropy systems, that is, tailorable composition and properties. The phase purity and solid solution nature of the molybdates were confirmed by XRD, Raman spectroscopy, TEM, XPS, and ICP OES.

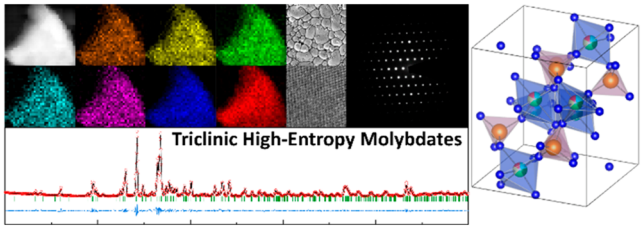

INTRODUCTION

The high entropy concept has been a topic of scientific research since the end of the 20th century.[1] The idea is to increase the configurational entropy (S_{config}) of a system so that the absolute value of the entropy dependent second term of the Gibbs−Helmholtz equation ($-T\Delta S$) increases, which in some cases can lead to an entropy stabilization of the structure. The absolute value of S_{config} is solely dependent on the number of different elements and their stoichiometry (eq S1 of the Supporting Information). Upon increasing S_{config}, by incorpo rating a multitude of elements in a single phase structure, manifold interactions between the different elements emerge, which can be seen as a characteristic of high entropy materials. These interactions often lead to unexpected and exciting properties compared to similar binary or ternary compounds. Additionally, it is possible to tailor the properties by simply changing the stoichiometry or the incorporated elements. The high entropy concept was first applied to alloys (HEAs) and later to ionic structures.[1,2] In 2015, Rost et al. synthesized the first entropy stabilized oxide and found clear signs of entropy mediated stabilization. They showed that reversible mixing and demixing of phases occurs when the temperature is increased and decreased, respectively. The single phase compound was thermodynamically favored only above a certain temperature, which is in agreement with the Gibbs−Helmholtz equation ($\Delta G = \Delta H - T\Delta S$).[3] Taking this into account, many high entropy materials can be described as metastable compounds that need to be quenched after high temperature synthesis to maintain a single phase structure. Today, there is a multitude of high entropy ceramics available, for example, oxides, borides, carbides, nitrides, sulfides, or silicides.[3−8] Their properties facilitate possible applications in the areas of energy storage, magnetism, thermal and environmental protection, thermoelectricity, water splitting, and catalysis, to name a few.[4,9−14] Apart from materials with simple anions, high entropy ceramics with complex anions like silicates (SiO_5^{6-}), disilicates ($Si_2O_7^{6-}$), diphosphates ($P_2O_7^{8-}$), and dizirconates ($Zr_2O_7^{6-}$) have also been presented.[9,15−17] Another class of interesting complex anions are the molybdates, which can form polyanions reaching from MoO_4^{2-} to $Mo_8O_{26}^{4-}$ and to even more complex structures.[18] Metal molybdates $MMoO_4$ (M = Ca, Fe, Co, Ni, Cd, Ba, etc.) have attracted scientific attention because of their catalytic, optical, photoluminescent, electro chemical, and magnetic properties.[19] For example, metal molybdates containing first row transition metals show promising catalytic properties because of the ability of the molybdenum ion and the respective transition metal ions to exist in multiple stable oxidation states.[20] Their catalytic activity enables different processes such as the selective oxidation of methanol or the reduction of nitrophenol isomers. Deng et al. reported about a certain kind of molybdenum containing high entropy oxide with desulfurization capabil ities.[21−23] Apart from the catalytic properties, copper molybdate can be used as a photocatalyst, and iron molybdate exhibits interesting ferromagnetic properties at room temper ature.[24,25] Furthermore, metal molybdates show promise for application in (super)capacitors and batteries.[26−28] Molyb

dates with "small" Mo numbers (e.g., MoO_4^{2-}, $Mo_2O_7^{2-}$, etc.) are composed of Mo^{6+} ions, tetrahedrally or octahedrally coordinated by oxygen ions (Figure S1). Compounds containing molybdates as anions often crystallize in structures of low symmetry. While $FeMoO_4$ shows a monoclinic ($C12/m1$) lattice, $ZnMoO_4$ forms a triclinic structure with the space group $P-1$ (Figure S1).[29,30] Other examples are monoclinic $MgMoO_4$ and $NiMoO_4$ or triclinic $CuMoO_4$.[31] Different methods have been used for the synthesis of transition metal molybdates, including hydrothermal/solvothermal, coprecipitation, sonochemical, combustion, sol–gel, and solid state routes.[24,25,27,32−35]

Here, we present, for the first time, the transfer of the high entropy concept to the triclinic molybdate system. So far, the symmetry of this compound class is the lowest ever reported for ionic high entropy ceramics. This is notable because high entropy materials usually tend to crystallize in highly symmetrical structures.[2,36−38] Metal molybdates with multiple metals in equimolar ratios were synthesized by utilizing an oxalate based coprecipitation method, followed by calcination at elevated temperatures. This synthesis method offers the possibility to produce several grams of powder and can be readily scaled up because of its simple reaction parameters (aqueous solution nonoptimized regarding pH value; readily available, nontoxic, and cheap precursors; no need to refine the products after calcination, etc.). The resultant powders are stable in air and moisture and do not react when handled at ambient conditions. A phase pure triclinic structure ($ZnMoO_4$ type, $P-1$) was obtained for two different compositions, namely $(MgNiCuZn)_1MoO_4$ and $(MgNiCuZnFe)_1MoO_4$, where the metals, except Mo, are incorporated in equimolar amounts. We expect that the introduction of the high entropy concept into molybdates paves the way for the development of compounds with different elemental compositions and tailorable properties for various applications.

EXPERIMENTAL SECTION

Synthesis. Two different high entropy materials were synthesized and characterized, namely $(MgNiCuZn)_1MoO_4$ and $(MgNiCuZnFe)_1MoO_4$, which are termed MEMo (medium entropy molybdate) and HEMo (high entropy molybdate), respectively. For the MEMo, a mixture (all >99%, Alfa Aesar) of acetate salts (5 mmol each) and MoO_3 (20 mmol) was dissolved or dispersed (MoO_3) into 150 mL of deionized water. The solution was stirred for around 15 min at room temperature and then heated to 90 °C. Subsequently, oxalic acid (>99%, Merck KGaA) solution (40 mmol in 50 mL of deionized water, molar ratio 1:1 in relation to the total metal concentration) was added dropwise at a rate of about 1 mL/min. The mixture was further stirred in a covered beaker for about 4 h at 90 °C. Then, the lid was removed to let the solvent evaporate overnight at the same temperature. The resulting solid was dried at 150 °C for 6 h and calcined for 4 h at 800 °C in air by using a muffle furnace, with subsequent quenching. The HEMo was similarly synthesized, but an adjusted molar ratio was used to acquire equimolar proportions of cations (4 mmol of each precursor added to 20 mmol of MoO_3) and $FeCl_2$ (>99%, Alfa Aesar) as additional precursor. An amount of about 4 g was obtained for both materials.

Structural Characterization. Powder X ray diffraction (XRD) data were collected by using a Bruker D8 diffractometer with Bragg–Brentano geometry and Cu $K\alpha_{1,2}$ radiation. Patterns were collected between 10° and 90° 2θ, with a step size of 0.02° and a scanning rate of 0.12°/min. Rietveld analysis was performed by using TOPAS Academics V5 software. The refinement was done with modifications to the elements and their proportion used in the respective samples, based on the structure type $ZnMoO_4$ (space group $P-1$, $Z = 6$).[39] The instrumental intensity distribution was determined by employing a reference scan of SRM 1976b (strain free Al_2O_3 in a glassy matrix, particle size >2 μm, random orientation).

The elements were determined and quantified by inductively coupled plasma optical emission spectroscopy (ICP OES, iCAP 7600DUO from Thermo Fisher Scientific). An amount of about 10 mg of the samples (weighing accuracy ±0.05 mg) was dissolved in 6 mL of hydrochloric acid, 2 mL of nitric acid, and 4 mL of sulfuric acid at 240 °C for 35 min by using a microwave oven (Speedwave Xpert from Berghof). Analysis of elements was accomplished with four different calibration solutions and an internal standard (Sc). Two or three major wavelengths of elements were used for calculation. The exact wavelengths can be seen in Table S1. The oxygen content was probed by the method of carrier gas hot extraction (CGHE). A commercial oxygen/nitrogen analyzer TC600 (LECO) was used. The maximum error margin for oxygen quantification is 0.7%.

The microstructure was analyzed via high resolution scanning electron microscopy (SEM, ZEISS Gemini Leo 1530). From the obtained images, the particle size and particle size distribution were determined by using the image processing program ImageJ.[41]

High resolution transmission electron microscopy (HR TEM), selected area electron diffraction (SAED), and and energy dispersive X ray spectroscopy (in scanning TEM mode, STEM EDX) data were collected by using an FEI Titan 80 300 microscope, equipped with a CEOS image spherical aberration corrector, a HAADF STEM detector (Fischione model 3000), an EDAX SUTW EDX detector, and a Tridiem Gatan image filter. An accelerating voltage of 300 kV was used. The powder samples were dispersed on a lacey carbon coated copper grid and loaded onto an FEI double tilt holder.

Raman spectroscopy was performed by using a Renishaw inVia Raman microscope. A 100× objective was used to focus the laser with a wavelength 532 nm, an exposure time of 10 s, a power of 2 mW, a numerical aperture of 0.8, and a working distance of 0.26 mm. The power of the collimated laser beam was measured in the microscope without the objective and then corrected for the specific objective transmission (~80%). The system was calibrated in a standard way by using a gas discharge lamp, using a software implemented routine. The absolute wavenumber accuracy of the Raman peak positions after this procedure is within ±0.5 cm^{-1}.

X ray photoelectron spectroscopy (XPS) measurements were performed on a K Alpha+ instrument (Thermo Fisher Scientific) with a monochromatic Al Kα X ray source (1486.6 eV) and a spot size of 400 μm. The K Alpha+ charge compensation system was applied to prevent localized charge buildup during analysis using 8 eV electrons and low energy Ar ions. Data acquisition and processing were performed by using Thermo Avantage software.[42] The spectra were fitted with one or more Voigt profiles. The binding energies are reported by considering the C 1s peak of hydrocarbons at 285.0 eV. The analyzer transmission function, Scofield sensitivity factors, and effective attenuation lengths (EALs) for photoelectrons were applied for quantification.[43] EALs were calculated by using the standard TPP 2 M formalism.[44] An error margin of ~10% is expected as quantification error for the Cu measurements.

RESULTS AND DISCUSSION

In this work, the synthesis and characterization of two multicomponent molybdates are presented: $Mg_{0.25}Ni_{0.25}Cu_{0.25}Zn_{0.25}MoO_4$ ($(MgNiCuZn)_1MoO_4$; medium entropy molybdate, MEMo) and $Mg_{0.2}Ni_{0.2}Cu_{0.2}Zn_{0.2}Fe_{0.2}MoO_4$ ($(MgNiCuZnFe)_1MoO_4$; high entropy molybdate, HEMo). The oxalate based coprecipitation method is a synthesis route enabling the preparation of triclinic high entropy molybdates. It can easily be scaled up to produce larger amounts of powder samples. Complex post treatments to form single phase structures, as known from other commonly used synthesis routes for high entropy materials, can be omitted. S_{config} calculation for MEMo and HEMo yielded 1.39R and 1.61R, respectively, which renders them medium and high entropy materials (eq S1). This classification is based on the often used

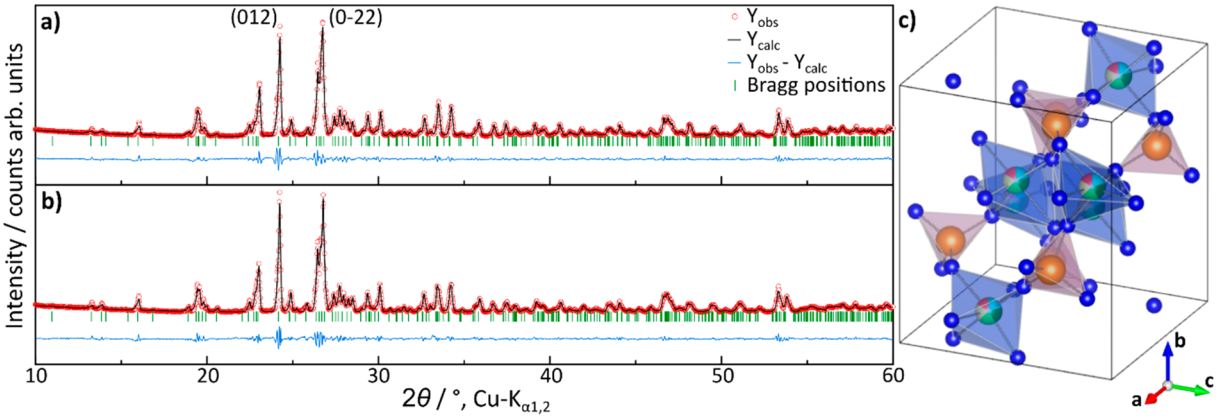

Figure 1. XRD patterns and related Rietveld refinement plots of (a) MEMo and (b) HEMo. (c) Model of the HEMo unit cell; the metal position can be occupied by Mg, Ni, Cu, Zn, or Fe (blue: O; orange: Mo; green: Mg; yellow: Ni; turquoise: Cu; dark green: Zn; red: Fe).[40]

condition that $S_{config} > 1.5R$ (R being the ideal gas constant) must be achieved to produce a high entropy material. Another condition is the equimolar ratio of metal species.[1] The crystal structure and phase composition of HEMo and MEMo were investigated by means of XRD and Rietveld refinement analysis. Figure S2 shows the XRD pattern of the triclinic reference material $Cu_{0.25}Zn_{0.75}MoO_4$ (ICSD 411380, $ZnMoO_4$ type, $P-1$) and the XRD patterns of the as prepared materials. The reflections of HEMo and MEMo match well with those reported for $Cu_{0.25}Zn_{0.75}MoO_4$. No other reflections were observed. Thus, it can be concluded that two phase pure triclinic materials were successfully synthesized. The refinement for both MEMo and HEMo is shown in Figure 1a,b, and the results are given in Table S2. For the distribution and calculation of the metal (M) occupancy on the cationic sublattice, it was assumed that the sites are completely and equally occupied by the metals (i.e., the sum is one). Both structures (MEMo and HEMo) contain MoO_4 tetrahedra, MO_6 octahedra, and trigonal bipyramidal MO_5 as characteristic building units (M = Mg, Ni, Cu, Zn, and Fe). Note that a parallel chain of MO_6 octahedra is arranged with connected trigonal MO_5 bipyramids and MoO_4 tetrahedra. As can be seen in Figure 1c, such a structure contains three dimensional channels through the lattice, which may positively affect the transport and/or charge storage properties.[27,45] The triclinic structure was rather unexpected because of the tendency of high entropy materials to crystallize in the highest symmetry possible.

In addition, the HEMo shows an intensity distribution of the two strongest reflections ((012) and (0−22) at 24.2° and 26.8°, respectively) similar to the reference material. In case of the MEMo, however, the intensity distribution was different. Similar behavior was found in the solid solution study of $Cu_{1-x}Zn_xMoO_4$. In this report, with increasing Zn content, an increase in intensity of the (0−22) reflection was observed, indicating direct occupation of the distorted Cu sites by Zn.[30] We assume that the HEMo shows a similar behavior and the addition of Fe leads to changes in electron density, resulting in the observed change in intensity of the reflections.

The lattice parameters and cell dimensions for all materials are virtually identical (Table S2). This is due to the average ionic radii of metals in HEMo and HEMo, which is close to that of Cu/Zn (Table S3). Thus, the lattice parameters a, b, c, β, and γ showed no significant differences between the MEMo and HEMo structures and the reference material. Only α showed a slightly lower value (by about 0.6°). Nevertheless, including the marginal changes of the other lattice parameters, this leads to a volume reduction by about 3 Å^3, which was somewhat expected based on the averaged ionic radius. The reflection positions of both synthesized materials shift to lower 2θ values for (012) and to larger values for (0−22) compared to the reference material. We assume that the unit cell is distorted because of the different sizes of ions (hence, we suppose that all ions are incorporated into the crystal lattice). This distortion results in reflection shifts, as indicated in Table S4.

The elemental composition was determined by ICP OES and CGHE. Table 1 reveals the composition of both samples in units of at. %. The theoretical ratio of constituent elements (assuming $M_1Mo_1O_4$) was nearly achieved. While for MEMo the ratio was $M_{0.99}Mo_{0.99}O_4$, the measurements on HEMo indicated a minor decrease in cation content ($M_{0.97}Mo_{0.96}O_4$). To achieve the highest S_{config} (see eq S1), it is necessary that all the transition metals are present in equimolar ratios. This prerequisite is achieved for both samples. The calculated formula based on the expected oxygen content of 4 is $(Mg_{0.25}Ni_{0.25}Cu_{0.25}Zn_{0.25})Mo_{0.99}O_4$ for the MEMo and $(Mg_{0.2}Ni_{0.19}Cu_{0.19}Zn_{0.19}Fe_{0.2})Mo_{0.96}O_4$ for the HEMo.

Table 1. Overview of the Elemental Compositions

element	MEMo [at. %]	HEMo [at. %]
Mg	4.1	3.3
Ni	4.1	3.3
Cu	4.2	3.2
Zn	4.1	3.2
Fe		3.3
Mo	16.6	16.3
O	66.8	67.4

The morphology of the HEMo can be seen in Figure 2. The SEM micrograph in Figure 2a shows that the material consists of agglomerates of different sizes, built from primary particles. The agglomerates are mostly compact and their diameters range between 5 and 100 μm. The (primary) particle size distribution, calculated by measuring 200 individual particles, is shown in Figure 2b. They appear to be nonuniform in shape (Figure 2c) and it should be noted that the shape is also affected to some degree by grain growth. A similar structure was found for the MEMo (Figure S3). The average size of

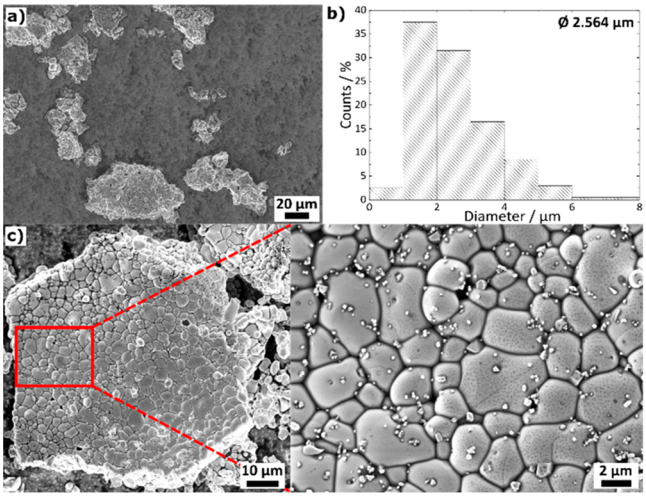

Figure 2. (a) SEM image of HEMo showing agglomerates of different sizes. (b) Size distribution of the primary particles displayed in (c). (c) SEM images at different magnifications of a single agglomerate (secondary particle).

primary particles is around 2.5 μm for both the HEMo and MEMo, and more than 65% of the particles are between 1 and 3 μm. The particle size distribution indicates that <5% of the particles are smaller than 1 μm or larger than 6 μm. It can be expected that other materials synthesized by using the same oxalate based coprecipitation approach will end up showing similar particle sizes. It is worth mentioning that there are also some nanoscale crystallites visible on the surface of the primary particles. Because of the relatively broad size distribution of agglomerates, it seems necessary to add a ball milling step before using the materials in specific applications.

Further microstructural details were obtained via TEM. Figure 3 shows HR TEM micrographs and the related SAED patterns of the MEMo and HEMo. Both materials show a high degree of crystallinity, as indicated by HR TEM (Figure 3a,b). Fast Fourier transforms (FFTs) of the respective areas are shown in the insets and support the observed triclinic structure. The distance between the visible diffraction planes in Figure 3a,b match with the values given in Figure 3c,d. The SAED reflections acquired from the corresponding areas of the HR TEM images correspond to the triclinic $Cu_{0.25}Zn_{0.75}MoO_4$ structure, as explained in the section on XRD above. For the MEMo material, the (−101), (−210), and (−11−1) lattice planes could be indexed using the d spacing and angles shown in Figure 3c. Likewise, the (−1−10), (−100), and (−110) lattice planes were indexed for the HEMo material (Figure 3d). The zone axis of the SAED in Figures 3c and 3d is [121] and [001], respectively.

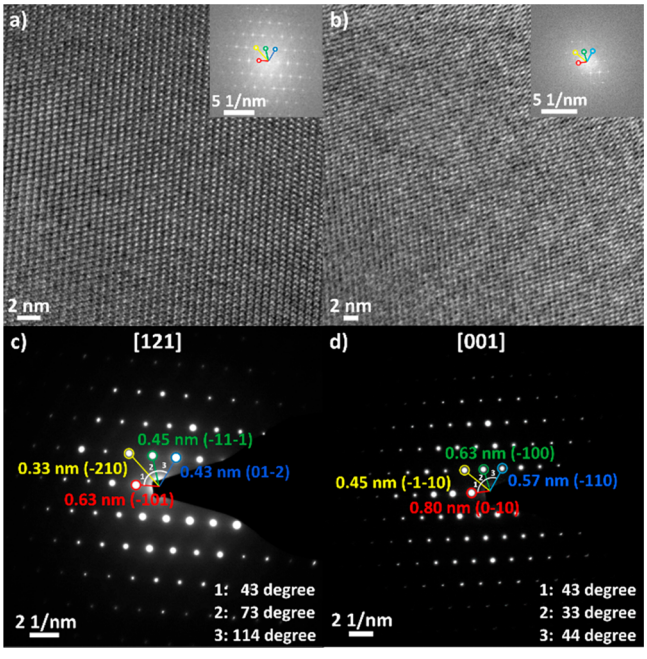

Figure 3. HR TEM images of (a) MEMo and (b) HEMo. Insets are FFTs of the HR TEM images. The marked indices in the FFTs are the same as in the SAED patterns of (c) MEMo and (d) HEMo.

STEM EDX was performed to examine the elemental distribution. Figure 4 shows the mapping results for the HEMo material. The pixel size is 10 nm. All elemental maps were processed by using the corresponding K edge. By comparison of the results in Figure 4, it is apparent that all elements show a homogeneous distribution, even in nano meter level resolution. There is no notable segregation or clustering, which would lead to a decrease in the number of possible microstates and therefore lower the configurational entropy.[46] A homogeneous distribution of all elements was also evident for the MEMo material (Figure S4).

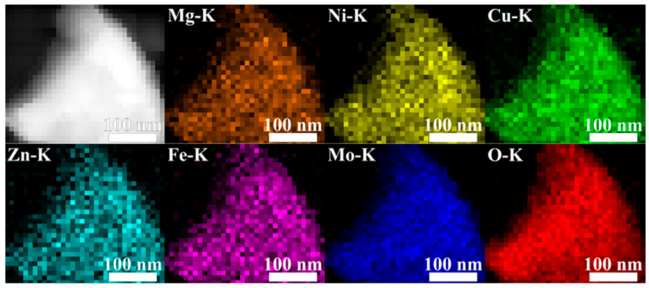

Figure 4. STEM image of the selected area used for EDX mapping of HEMo. The uniform distribution of Mg, Ni, Cu, Zn, Fe, Mo, and O is apparent.

Raman spectroscopy measurements were performed on the MEMo and HEMo because transition metal molybdates are known to be Raman active, and the spectra provide structural details on local molecular vibrations.[47] Figure 5 shows the Raman spectra of MEMo and HEMo, with the shaded areas denoting regions of different vibrational modes. Region A reveals a characteristic band at 291−350 cm^{-1}, corresponding to the O−Mo−O bending, while those in region B (781−821 cm^{-1}) and region C (935−962 cm^{-1}) correspond to the antisymmetric and symmetric stretching modes of the MoO_4 tetrahedra, respectively.[48−50] The different modes superimposed in region B indicate a noncentrosymmetric occupation of the MoO_4 tetrahedra; related softening of exclusion rules leads to appearance of different Raman bands. The broadening of bands in region C for MEMo is assumed to be due to structural disorder.

XPS was used to determine the oxidation states of the metals on the surface of the MEMo and HEMo. In Figure 6, the Mo 3d spectrum exhibits one spin−orbit doublet with Mo $3d_{5/2}$ at 232.6 eV and a doublet splitting of 3.2 eV for MEMo and HEMo. According to the binding energy and narrow full width at half maximum (FWHM: 1.1 eV) of the Mo 3d doublet, Mo

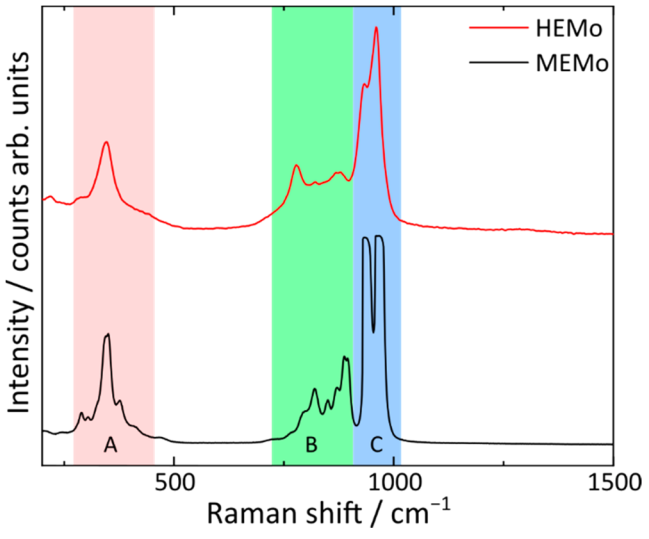

Figure 5. Raman spectra of MEMo and HEMo. The colored regions denote different vibration modes. A: O−Mo−O bending; B: antisymmetric stretching of MoO_4 tetrahedra; C: symmetric stretching modes of MoO_4 tetrahedra.

ions can be assigned to Mo^{6+}, supported by the literature.[51−54] The binding energy of lattice oxygen is determined to be 530.7 eV, and very little carbonates or hydroxides are formed on the surface, according to the C 1s and O 1s spectra shown in Figure S5. The oxidation state of Mg, Zn, and Ni in the MEMo and HEMo is determined to be 2+. The Mg 1s and Mg 2p binding energies at 1304.1 and 50.0 eV, respectively (as well as Mg KLL with a binding energy of ∼304.2 eV), are indicative of Mg^{2+} (Figure 6 and Figure S5).[55−57] Figure 7 reveals that the Zn ions (with Zn $2p_{3/2}$ binding energy of 1021.8 eV and Zn LMM kinetic energy of ∼988.6 eV) are in the oxidation state 2+.[57,58] In Figure 6, the multiplet deconvolution of the Ni $2p_{3/2}$ spectra is shown. The fit was realized with minor intensity ratio variations in multiplets of Ni^{2+}.[57,59−62] The multiplet splitting effect of Ni ions and the difficulty of identification of their oxidation state solely based on the peak barycenter have already been reported.[58,63,64]

The spectra of Cu ions of the MEMo and HEMo in Figure 7 show a complicated structure. It is known that Cu^{2+} ions in oxide materials can easily be reduced to Cu^{1+} and Cu^0 by extended exposure to X rays; therefore, in these measurements, the Cu ions are probed at the start of the experiment with only 3 min of total X ray exposure to prevent degradation.[58,65] Hence, we assume that the low binding energy peak of Cu $2p_{3/2}$ (A_{932}) at 932.5 eV (FWHM: 2.0 eV) can be attributed to either Cu^{1+} or Cu^0. Note that binding energy values for Cu metal and Cu(I) oxide represent statistically similar values, and their differentiation can be done usually by considering the Cu LMM peak. However, the detailed evaluation of the X ray induced Cu Auger peaks in these materials is hampered by the overlap of low intensity Zn LMM peaks.[58] This makes the speciation of the A_{932} peak based on the Auger parameter difficult. We carefully assign the A_{932} peak to Cu^{1+} because of its relatively large FWHM (2 eV) and appearance of the Cu $L_3M_{4,5}M_{4,5}$ peak at the kinetic energy of 916.4 eV, close to the value found for Cu(I) species.[66] The middle main peak in the Cu $2p_{3/2}$ spectrum (B_{935}) with a binding energy of 934.7 eV (for MEMo) and 935.1 eV (for HEMo) is identified as Cu^{2+}, which also gives rise to the observed shake up satellite peaks in the spectrum. The origin of the third main peak (C_{937}) at ∼936.8 eV is unknown. Note that we exclude the possibility of overlapping Fe LMM Auger because this peak is also present for the sample without Fe. Studies on the ratio of the satellite peak to main peak area in $Cu(OH)_2$ and CuO have shown values around 1.6 and 1.9, respectively.[58] In case of the MEMo and HEMo, the ratio of satellites peak area to sum of peaks at ∼935 and ∼937 eV is ∼1.55, which is close to the ratio

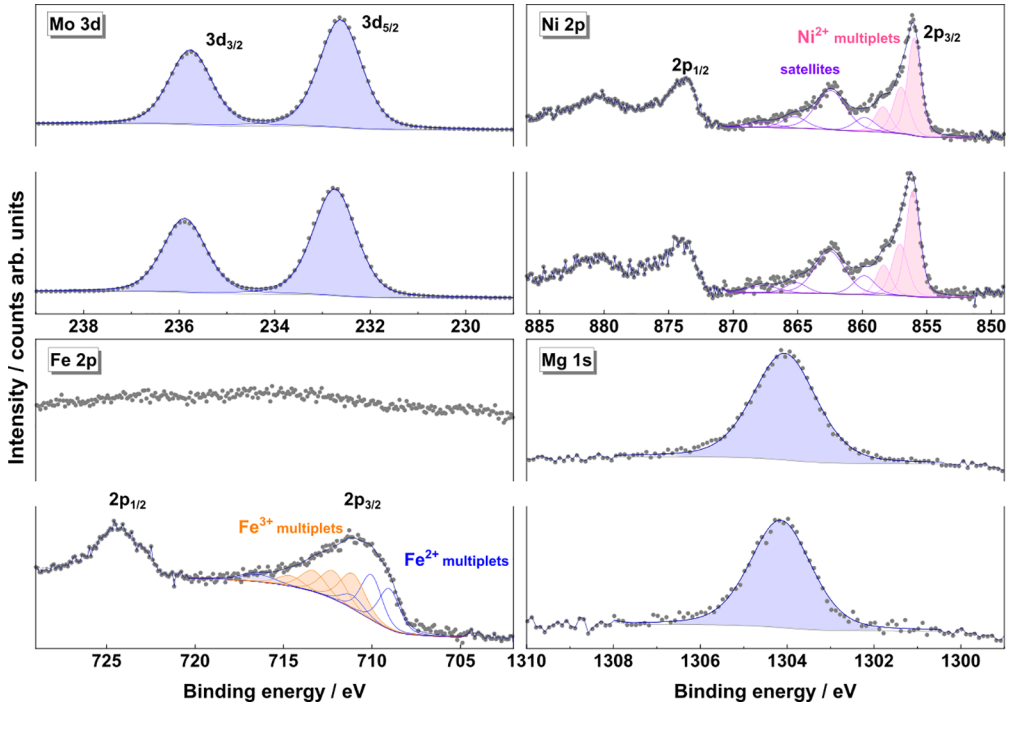

Figure 6. XP spectra of MEMo (top) and HEMo (bottom) showing the Mo 3d, Ni 2p, Fe 2p, and Mg 1s peaks.

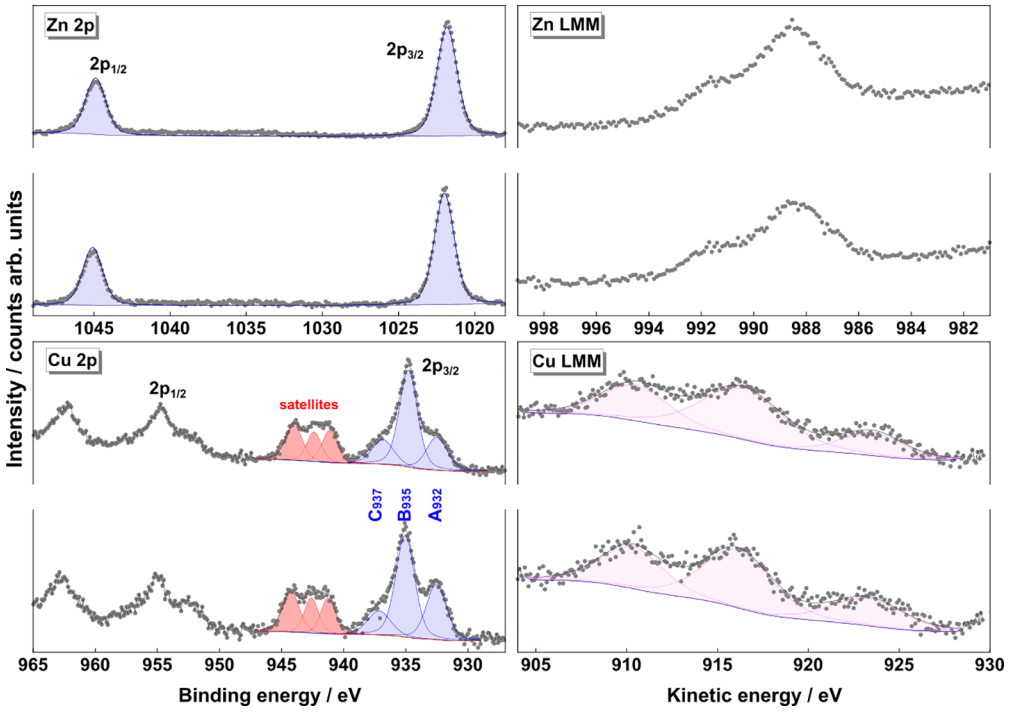

Figure 7. XP spectra of MEMo (top) and HEMo (bottom) showing the Zn 2p, Zn LMM, Cu 2p, and Cu LMM peaks.

obtained for $Cu(OH)_2$. This leads us to speculatively attribute both B_{935} and C_{937} peaks to Cu^{2+}. In summary, the amount of Cu^{1+} can be determined to be 15% and 21% of the total Cu ions for the MEMo and HEMo, respectively. Therefore, the average Cu oxidation state is estimated at $Cu^{1.8+}$ ($Cu^{1.85+}$ for MEMo and $Cu^{1.79+}$ for HEMo).

Finally, the Fe 2p spectrum of HEMo shows its doublet structure with broad peaks because of multiplet splitting and the presence of shake up satellites. The average oxidation state of the Fe ions, according to the presented multiplet splitting deconvolution of the Fe $2p_{3/2}$ spectra in Figure 6, is close to 2.5+, considering the percentage of Fe^{3+} (orange multiplets) and Fe^{2+} (blue multiplets) is 50.7% and 49.3% of the total Fe ions, respectively.[57,58,67] However, the overall oxidation state is slightly higher than the expected value of 2+. An overview of all oxidation states is presented in Table 2. It is known in the literature that Cu often takes lower oxidation states when combined with other transition metals in one compound, leading to an oxidation of the respective metal ion.[68,69] We assume that this internal disproportionation ($Cu^{2+} + M^{2+} \rightarrow Cu^{+} + M^{3+}$) is also occurring in the MEMo and HEMo. Because Mg and Zn appear only in 2+ state, the possible reaction partners for Cu are Ni in the MEMo and Ni and Fe in the HEMo. To reduce the Cu^{2+} in the MEMo to an average of $Cu^{1.85+}$, only 15% of the incorporated Ni must be oxidized, which might be difficult to resolve as explained above.[63,64] The increased reduction of Cu in the HEMo can be attributed to the additional oxidation of Fe. Nevertheless, this mechanism alone cannot explain the oxidation of almost 50% Fe by reduction of ~20% Cu. We assume that cation vacancies lead to the higher than expected oxidation state of Fe, since otherwise, because of the necessity to maintain charge neutrality, other cations would have to compensate for the charge. Note that a reduction of Cu^{2+} to Cu^{+} by X ray exposure, although the exposure time was minimized, cannot be fully excluded. Additionally, the described redox process for the MEMo is not straightforward and leaves some open questions. Nevertheless, we do not expect that all Cu^{2+} reduction processes are derived from X ray reduction; therefore, this might be the only possible option. ICP OES/CGHE results indicate that the HEMo incorporates more cation vacancies than the MEMo; the cation:anion ratio is slightly lower for the HEMo (meaning fewer cations per anion; therefore, vacancies must exist in the lattice). The measured surface stoichiometry agrees well with the bulk stoichiometry (Table S5 and Table 2).

Table 2. Overview of the Elemental Compositions from ICP OES/CGHE and Oxidation States from XPS

	MEMo		HEMo	
element	composition [at. %]	oxidation state	composition [at. %]	oxidation state
Mg	4.1	2+	3.3	2+
Ni	4.1	2+	3.3	2+
Cu	4.2	1.85+	3.2	1.79+
Zn	4.1	2+	3.2	2+
Fe			3.3	2.5+
Mo	16.6	6+	16.3	6+
O	66.8		67.4	

CONCLUSIONS

Two single phase high entropy materials, a medium and a high entropy molybdate, showing triclinic $ZnMoO_4$ type structure ($P\bar{1}$), were successfully produced by using a wet chemical based synthesis approach. These compounds show solid solution characteristics with homogeneously distributed metal cations (Mg, Ni, Cu, Zn, and Fe) and tetrahedral MoO_4 units. Both materials possess a high degree of crystallinity and long range order without any indications of the presence of secondary phases. The synthesis route allows for facile

upscaling and may pave the way for the easy preparation of novel classes of high entropy materials.

AUTHOR INFORMATION

Corresponding Authors

Ben Breitung − *Institute of Nanotechnology, Karlsruhe Institute of Technology (KIT), 76344 Eggenstein Leopoldshafen, Germany;* orcid.org/0000 0002 1304 3398; Email: ben.breitung@kit.edu

Simon Schweidler − *Institute of Nanotechnology, Karlsruhe Institute of Technology (KIT), 76344 Eggenstein Leopoldshafen, Germany;* orcid.org/0000 0003 4675 1072; Email: simon.schweidler@kit.edu

Authors

David Stenzel − *Institute of Nanotechnology, Karlsruhe Institute of Technology (KIT), 76344 Eggenstein Leopoldshafen, Germany*

Ibrahim Issac − *Institute of Nanotechnology, Karlsruhe Institute of Technology (KIT), 76344 Eggenstein Leopoldshafen, Germany*

Kai Wang − *Institute of Nanotechnology, Karlsruhe Institute of Technology (KIT), 76344 Eggenstein Leopoldshafen, Germany*

Raheleh Azmi − *Institute for Applied Materials – Energy Storage Systems, Karlsruhe Institute of Technology (KIT), 76344 Eggenstein Leopoldshafen, Germany*

Ruby Singh − *Institute of Nanotechnology, Karlsruhe Institute of Technology (KIT), 76344 Eggenstein Leopoldshafen, Germany*

Jaehoon Jeong − *Institute of Nanotechnology, Karlsruhe Institute of Technology (KIT), 76344 Eggenstein Leopoldshafen, Germany*

Saleem Najib − *Faculty of Engineering, University of Waterloo, Waterloo, Ontario N2L 3G1, Canada*

Subramshu S. Bhattacharya − *Department of Metallurgical and Materials Engineering, Nano Functional Materials Technology Centre (NFMTC), Indian Institute of Technology Madras, Chennai 600036, India;* orcid.org/0000 0002 6865 0822

Horst Hahn − *Institute of Nanotechnology, Karlsruhe Institute of Technology (KIT), 76344 Eggenstein Leopoldshafen, Germany; Joint Research Laboratory Nanomaterials, Technical University Darmstadt, 64206 Darmstadt, Germany; Helmholtz Institute Ulm for Electrochemical Energy Storage, 89081 Ulm, Germany;* orcid.org/0000 0001 9901 3861

Torsten Brezesinski − *Institute of Nanotechnology, Karlsruhe Institute of Technology (KIT), 76344 Eggenstein Leopoldshafen, Germany;* orcid.org/0000 0002 4336 263X

Notes

The authors declare no competing financial interest.

ACKNOWLEDGMENTS

H.H. acknowledges financial support from the Helmholtz Association and the German Research Foundation (HA 1344/43 1). D.S. and B.B. appreciate the support of EnABLES, a project funded by the European Union's Horizon 2020 research and innovation program under grant agreement no. 730957. This work contributes to the research performed at CELEST (Center for Electrochemical Energy Storage Ulm Karlsruhe) and was funded by the German Research Foundation under Project ID 390874152 (POLiS Cluster of Excellence). S.N. thanks the Christian Bürkert Foundation for funding. The authors acknowledge the support from the Karlsruhe Nano Micro Facility (KNMF, www.knmf.kit.edu), a Helmholtz research infrastructure at Karlsruhe Institute of Technology (KIT, www.kit.edu). Dr. Thomas Bergfeldt (from IAM AWP, KIT) is acknowledged for ICP OES and CGHE measurements. The authors thank Qingsong Wang for fruitful discussions.

REFERENCES

(1) Murty, B. S.; Yeh, J. W.; Ranganathan, S.; Bhattacharjee, P. P. *High Entropy Alloys*, 2nd ed.; Elsevier Science: 2019.

(2) Oses, C.; Toher, C.; Curtarolo, S. High Entropy Ceramics. *Nat. Rev. Mater.* **2020**, *5* (4), 295−309.

(3) Rost, C. M.; Sachet, E.; Borman, T.; Moballegh, A.; Dickey, E. C.; Hou, D.; Jones, J. L.; Curtarolo, S.; Maria, J. P. Entropy Stabilized Oxides. *Nat. Commun.* **2015**, *6* (1), 8485.

(4) Zhang, R. Z.; Gucci, F.; Zhu, H.; Chen, K.; Reece, M. J. Data Driven Design of Ecofriendly Thermoelectric High Entropy Sulfides. *Inorg. Chem.* **2018**, *57* (20), 13027−13033.

(5) Jin, T.; Sang, X.; Unocic, R. R.; Kinch, R. T.; Liu, X.; Hu, J.; Liu, H.; Dai, S. Mechanochemical Assisted Synthesis of High Entropy Metal Nitride via a Soft Urea Strategy. *Adv. Mater.* **2018**, *30* (23), 1707512.

(6) Gild, J.; Zhang, Y.; Harrington, T.; Jiang, S.; Hu, T.; Quinn, M. C.; Mellor, W. M.; Zhou, N.; Vecchio, K.; Luo, J. High Entropy Metal Diborides: A New Class of High Entropy Materials and a New Type of Ultrahigh Temperature Ceramics. *Sci. Rep.* **2016**, *6* (1), 37946.

(7) Sarker, P.; Harrington, T.; Toher, C.; Oses, C.; Samiee, M.; Maria, J. P.; Brenner, D. W.; Vecchio, K. S.; Curtarolo, S. High Entropy High Hardness Metal Carbides Discovered by Entropy Descriptors. *Nat. Commun.* **2018**, *9* (1), 4980.

(8) Gild, J.; Braun, J.; Kaufmann, K.; Marin, E.; Harrington, T.; Hopkins, P.; Vecchio, K.; Luo, J. A High Entropy Silicide: $(Mo_{0.2}Nb_{0.2}Ta_{0.2}Ti_{0.2}W_{0.2})Si_2$. *J. Mater.* **2019**, *5* (3), 337−343.

(9) Dong, Y.; Ren, K.; Lu, Y.; Wang, Q.; Liu, J.; Wang, Y. High Entropy Environmental Barrier Coating for the Ceramic Matrix Composites. *J. Eur. Ceram. Soc.* **2019**, *39* (7), 2574−2579.

(10) Li, F.; Zhou, L.; Liu, J. X.; Liang, Y.; Zhang, G. J. High Entropy Pyrochlores with Low Thermal Conductivity for Thermal Barrier Coating Materials. *J. Adv. Ceram.* **2019**, *8* (4), 576−582.
(11) Zhai, S.; Rojas, J.; Ahlborg, N.; Lim, K.; Toney, M. F.; Jin, H.; Chueh, W. C.; Majumdar, A. The Use of Poly Cation Oxides to Lower the Temperature of Two Step Thermochemical Water Splitting. *Energy Environ. Sci.* **2018**, *11* (8), 2172−2178.
(12) Sarkar, A.; Wang, Q.; Schiele, A.; Chellali, M. R.; Bhattacharya, S. S.; Wang, D.; Brezesinski, T.; Hahn, H.; Velasco, L.; Breitung, B. High Entropy Oxides: Fundamental Aspects and Electrochemical Properties. *Adv. Mater.* **2019**, *31* (26), 1806236.
(13) Wang, J.; Cui, Y.; Wang, Q.; Wang, K.; Huang, X.; Stenzel, D.; Sarkar, A.; Azmi, R.; Bergfeldt, T.; Bhattacharya, S. S.; Kruk, R.; Hahn, H.; Schweidler, S.; Brezesinski, T.; Breitung, B. Lithium Containing Layered High Entropy Oxide Structures. *Sci. Rep.* **2020**, *10*, 18430.
(14) Wang, Q.; Sarkar, A.; Wang, D.; Velasco, L.; Azmi, R.; Bhattacharya, S. S.; Bergfeldt, T.; Düvel, A.; Heitjans, P.; Brezesinski, T.; Hahn, H.; Breitung, B. Multi Anionic and Cationic Compounds: New High Entropy Materials for Advanced Li Ion Batteries. *Energy Environ. Sci.* **2019**, *12*, 2433−2442.
(15) Ren, X.; Tian, Z.; Zhang, J.; Wang, J. Equiatomic Quaternary $(Y_{1/4}Ho_{1/4}Er_{1/4}Yb_{1/4})_2SiO_5$ Silicate: A Perspective Multifunctional Thermal and Environmental Barrier Coating Material. *Scr. Mater.* **2019**, *168*, 47−50.
(16) Zhao, Z.; Xiang, H.; Dai, F. Z.; Peng, Z.; Zhou, Y. $(TiZrHf)P_2O_7$: An Equimolar Multicomponent or High Entropy Ceramic with Good Thermal Stability and Low Thermal Con ductivity. *J. Mater. Sci. Technol.* **2019**, *35* (10), 2227−2231.
(17) Zhao, Z.; Xiang, H.; Dai, F. Z.; Peng, Z.; Zhou, Y. $(La_{0.2}Ce_{0.2}Nd_{0.2}Sm_{0.2}Eu_{0.2})_2Zr_2O_7$: A Novel High Entropy Ceramic with Low Thermal Conductivity and Sluggish Grain Growth Rate. *J. Mater. Sci. Technol.* **2019**, *35* (11), 2647−2651.
(18) Kitamura, A.; Ozeki, T.; Yagasaki, A. β Octamolybdate as a Building Block. Synthesis and Structural Characterization of Rare Earth−Molybdate Adducts. *Inorg. Chem.* **1997**, *36* (19), 4275−4279.
(19) Wang, W. S.; Zhen, L.; Xu, C. Y.; Shao, W. Z. Room Temperature Synthesis, Growth Mechanism, Photocatalytic and Photoluminescence Properties of Cadmium Molybdate Core Shell Microspheres. *Cryst. Growth Des.* **2009**, *9* (3), 1558−1568.
(20) Velasquez, J.; Echavarria, A.; Faro, A.; Palacio, L. A. Propane Oxidative Dehydrogenation on ZnCoMo and NiCoMo Catalysts Obtained from Φ_y and Φ_x Precursors. *Ind. Eng. Chem. Res.* **2013**, *52* (16), 5582−5586.
(21) Bowker, M.; Holroyd, R.; House, M.; Bracey, R.; Bamroongwongdee, C.; Shannon, M.; Carley, A. The Selective Oxidation of Methanol on Iron Molybdate Catalysts. *Top. Catal.* **2008**, *48* (1−4), 158−165.
(22) Oudghiri Hassani, H.; Al Wadaani, F. Preparation, Character ization and Catalytic Activity of Nickel Molybdate ($NiMoO_4$) Nanoparticles. *Molecules* **2018**, *23* (2), 273.
(23) Deng, C.; Wu, P.; Zhu, L.; He, J.; Tao, D. J.; Lu, L.; He, M.; Hua, M.; Li, H.; Zhu, W. High Entropy Oxide Stabilized Molybdenum Oxide via High Temperature for Deep Oxidative Desulfurization. *Appl. Mater. Today* **2020**, *20*, 100680.
(24) Sadeghi, M. Investigation of the Structural, Optical and Magnetic Properties of $CuMoO_4$ Nanoparticles Synthesized through a Sonochemical Method. *J. Mater. Sci.: Mater. Electron.* **2016**, *27* (6), 5796−5801.
(25) Zhang, Z.; Hu, C.; Hashim, M.; Chen, P.; Xiong, Y.; Zhang, C. Synthesis and Magnetic Property of $FeMoO_4$ Nanorods. *Mater. Sci. Eng., B* **2011**, *176* (9), 756−761.
(26) Reddy, B. J.; Vickraman, P.; Justin, A. S. A Facile Synthesis of Novel α $ZnMoO_4$ Microspheres as Electrode Material for Super capacitor Applications. *Bull. Mater. Sci.* **2019**, *42* (2), 52.
(27) Devi, M.; Varadaraju, U. V. Lithium Insertion in Lithium Iron Molybdate. *Electrochem. Commun.* **2012**, *18* (1), 112−115.
(28) Haetge, J.; Suchomski, C.; Brezesinski, T. Ordered Mesoporous β $MgMoO_4$ Thin Films for Lithium Ion Battery Applications. *Small* **2013**, *9* (15), 2541−2544.
(29) Sleight, A. W.; Chamberland, B. L.; Weiher, J. F. Magnetic, Moessbauer, and Structural Studies on Three Modifications of $FeMoO_4$. *Inorg. Chem.* **1968**, *7* (6), 1093−1098.
(30) Reichelt, W.; Weber, T.; Söhnel, T.; Däbritz, S. Mischkris tallbildung Im System $CuMoO_4/ZnMoO_4$. *Z. Anorg. Allg. Chem.* **2000**, *626* (9), 2020−2027.
(31) Sleight, A. W.; Chamberland, B. L. Transition Metal Molybdates of the Type $AMoO_4$. *Inorg. Chem.* **1968**, *7* (8), 1672−1675.
(32) Zhang, Z.; Li, W.; Ng, T. W.; Kang, W.; Lee, C. S.; Zhang, W. Iron(II) Molybdate ($FeMoO_4$) Nanorods as a High Performance Anode for Lithium Ion Batteries: Structural and Chemical Evolution upon Cycling. *J. Mater. Chem. A* **2015**, *3* (41), 20527−20534.
(33) Kim, S. Reaction Mechanisms of $MnMoO_4$ for High Capacity Anode Material of Li Secondary Battery. *Solid State Ionics* **2002**, *146* (3−4), 249−256.
(34) Ramezani, M.; Hosseinpour Mashkani, S. M.; Sobhani Nasab, A.; Ghasemi Estarki, H. Synthesis, Characterization, and Morpho logical Control of $ZnMoO_4$ Nanostructures through Precipitation Method and Its Photocatalyst Application. *J. Mater. Sci.: Mater. Electron.* **2015**, *26* (10), 7588−7594.
(35) Sekar, C.; Selvan, R. K.; Senthilkumar, S. T.; Senthilkumar, B.; Sanjeeviraja, C. Combustion Synthesis and Characterization of Spherical α $MnMoO_4$ Nanoparticles. *Powder Technol.* **2012**, *215−216* (3), 98−103.
(36) Djenadic, R.; Sarkar, A.; Clemens, O.; Loho, C.; Botros, M.; Chakravadhanula, V. S. K.; Kübel, C.; Bhattacharya, S. S.; Gandhi, A. S.; Hahn, H. Multicomponent Equiatomic Rare Earth Oxides. *Mater. Res. Lett.* **2017**, *5* (2), 102−109.
(37) Sarkar, A.; Djenadic, R.; Usharani, N. J.; Sanghvi, K. P.; Chakravadhanula, V. S. K.; Gandhi, A. S.; Hahn, H.; Bhattacharya, S. S. Nanocrystalline Multicomponent Entropy Stabilised Transition Metal Oxides. *J. Eur. Ceram. Soc.* **2017**, *37* (2), 747−754.
(38) Sarkar, A.; Djenadic, R.; Wang, D.; Hein, C.; Kautenburger, R.; Clemens, O.; Hahn, H. Rare Earth and Transition Metal Based Entropy Stabilised Perovskite Type Oxides. *J. Eur. Ceram. Soc.* **2018**, *38* (5), 2318−2327.
(39) Weber, T.; Harz, M.; Wehner, B.; Zahn, G.; Paufler, P. Thermal Expansion of $CuMoO_4$ below Room Temperature. *Z. Kristallogr. Cryst. Mater.* **1998**, *213* (4).
(40) Momma, K.; Izumi, F. VESTA 3 for Three Dimensional Visualization of Crystal, Volumetric and Morphology Data. *J. Appl. Crystallogr.* **2011**, *44* (6), 1272−1276.
(41) Schneider, C. A.; Rasband, W. S.; Eliceiri, K. W. NIH Image to ImageJ: 25 Years of Image Analysis. *Nat. Methods* **2012**, *9* (7), 671−675.
(42) Parry, K. L.; Shard, A. G.; Short, R. D.; White, R. G.; Whittle, J. D.; Wright, A. ARXPS Characterisation of Plasma Polymerised Surface Chemical Gradients. *Surf. Interface Anal.* **2006**, *38* (11), 1497−1504.
(43) Scofield, J. H. Hartree Slater Subshell Photoionization Cross Sections at 1254 and 1487 EV. *J. Electron Spectrosc. Relat. Phenom.* **1976**, *8* (2), 129−137.
(44) Tanuma, S.; Powell, C. J.; Penn, D. R. Calculations of Electron Inelastic Mean Free Paths. IX. Data for 41 Elemental Solids over the 50 EV to 30 KeV Range. *Surf. Interface Anal.* **2011**, *43* (3), 689−713.
(45) Padhi, A. K.; Nanjundaswamy, K. S.; Goodenough, J. B. Phospho Olivines as Positive Electrode Materials for Rechargeable Lithium Batteries. *J. Electrochem. Soc.* **1997**, *144* (4), 1188.
(46) Chellali, M. R.; Sarkar, A.; Nandam, S. H.; Bhattacharya, S. S.; Breitung, B.; Hahn, H.; Velasco, L. On the Homogeneity of High Entropy Oxides: An Investigation at the Atomic Scale. *Scr. Mater.* **2019**, *166*, 58−63.
(47) Tian, H.; Wachs, I. E.; Briand, L. E. Comparison of UV and Visible Raman Spectroscopy of Bulk Metal Molybdate and Metal Vanadate Catalysts. *J. Phys. Chem. B* **2005**, *109* (49), 23491−23499.
(48) Haetge, J.; Djerdj, I.; Brezesinski, T. Nanocrystalline $NiMoO_4$ with an Ordered Mesoporous Morphology as Potential Material for

Rechargeable Thin Film Lithium Batteries. *Chem. Commun.* **2012**, *48*, 6726−6728.
(49) Ait Ahsaine, H.; Zbair, M.; Ezahri, M.; Benlhachemi, A.; Bakiz, B.; Guinneton, F.; Gavarri, J. R. Structural and Temperature Dependent Vibrational Analyses of the Non Centrosymmetric $ZnMoO_4$ Molybdate. *J. Mater. Environ. Sci.* **2016**, *7* (9), 3076−3083.
(50) Tan, W.; Luan, J. Investigation into the Synthesis Conditions of $CuMoO_4$ by an: In Situ Method and Its Photocatalytic Properties under Visible Light Irradiation. *RSC Adv.* **2020**, *10* (16), 9745−9759.
(51) Werfel, F.; Minni, E. Photoemission Study of the Electronic Structure of Mo and Mo Oxides. *J. Phys. C: Solid State Phys.* **1983**, *16* (31), 6091−6100.
(52) Brox, B.; Olefjord, I. ESCA Studies of MoO_2 and MoO_3. *Surf. Interface Anal.* **1988**, *13* (1), 3−6.
(53) Ho, S. F.; Contarini, S.; Rabalais, J. W. Metallization Channels in Ion Induced Decomposition of Molybdates and Niobates. *Chem. Phys. Lett.* **1987**, *133* (2), 171−175.
(54) Baltrusaitis, J.; Mendoza sanchez, B.; Fernandez, V.; Veenstra, R.; Dukstiene, N.; Roberts, A.; Fairley, N. Applied Surface Science Generalized Molybdenum Oxide Surface Chemical State XPS Determination via Informed Amorphous Sample Model. *Appl. Surf. Sci.* **2015**, *326*, 151−161.
(55) Diler, E.; Lescop, B.; Rioual, S.; Nguyen Vien, G.; Thierry, D.; Rouvellou, B. Initial Formation of Corrosion Products on Pure Zinc and $MgZn_2$ Examinated by XPS. *Corros. Sci.* **2014**, *79*, 83−88.
(56) Mittal, V. K.; Chandramohan, P.; Bera, S.; Srinivasan, M. P.; Velmurugan, S.; Narasimhan, S. V. Cation Distribution in $Ni_xMg_{1-x}Fe_2O_4$ Studied by XPS and Mössbauer Spectroscopy. *Solid State Commun.* **2006**, *137* (1−2), 6−10.
(57) Wang, J.; Stenzel, D.; Azmi, R.; Najib, S.; Wang, K.; Jeong, J.; Sarkar, A.; Wang, Q.; Sukkurji, P. A.; Bergfeldt, T.; Botros, M.; Maibach, J.; Hahn, H.; Brezesinski, T.; Breitung, B. Spinel to Rock Salt Transformation in High Entropy Oxides with Li Incorporation. *Electrochem* **2020**, *1* (1), 60−74.
(58) Biesinger, M. C.; Payne, B. P.; Grosvenor, A. P.; Lau, L. W. M.; Gerson, A. R.; Smart, R. S. C. Resolving Surface Chemical States in XPS Analysis of First Row Transition Metals, Oxides and Hydroxides: Cr, Mn, Fe, Co and Ni. *Appl. Surf. Sci.* **2011**, *257* (7), 2717−2730.
(59) Mariappan, C. R.; Kumar, V.; Azmi, R.; Esmezjan, L.; Indris, S.; Bruns, M.; Ehrenberg, H. High Electrochemical Performance of 3D Highly Porous $Zn_{0.2}Ni_{0.8}Co_2O_4$ Microspheres as an Electrode Material for Electrochemical Energy Storage. *CrystEngComm* **2018**, *20* (15), 2159−2168.
(60) Azmi, R.; Masoumi, M.; Ehrenberg, H.; Trouillet, V.; Bruns, M. Surface Analytical Characterization of $LiNi_{0.8-y}Mn_yCo_{0.2}O_2$ ($0 \leq y \leq 0.4$) Compounds for Lithium Ion Battery Electrodes. *Surf. Interface Anal.* **2018**, *50* (11), 1132−1137.
(61) Azmi, R.; Trouillet, V.; Strafela, M.; Ulrich, S.; Ehrenberg, H.; Bruns, M. Surface Analytical Approaches to Reliably Characterize Lithium Ion Battery Electrodes. *Surf. Interface Anal.* **2018**, *50* (1), 43−51.
(62) Kumar, V.; Mariappan, C. R.; Azmi, R.; Moock, D.; Indris, S.; Bruns, M.; Ehrenberg, H.; Vijaya Prakash, G. Pseudocapacitance of Mesoporous Spinel Type MCo_2O_4 (M = Co, Zn, and Ni) Rods Fabricated by a Facile Solvothermal Route. *ACS Omega* **2017**, *2* (9), 6003−6013.
(63) Biesinger, M. C.; Payne, B. P.; Lau, L. W. M.; Gerson, A.; Smart, R. S. C. X Ray Photoelectron Spectroscopic Chemical State Quantification of Mixed Nickel Metal, Oxide and Hydroxide Systems. *Surf. Interface Anal.* **2009**, *41* (4), 324−332.
(64) Grosvenor, A. P.; Biesinger, M. C.; Smart, R. S. C.; McIntyre, N. S. New Interpretations of XPS Spectra of Nickel Metal and Oxides. *Surf. Sci.* **2006**, *600* (9), 1771−1779.
(65) Marletta, G.; Puglisi, O.; Pignataro, S.; Albert, G.; Costantino, U. X Ray Induced Cu(II) Reductions in α and γ Zirconium Phosphates Intercalated with Copper Ions. *Chem. Phys. Lett.* **1982**, *89* (4), 333−336.
(66) Kirsch, P. D.; Ekerdt, J. G. Chemical and Thermal Reduction of Thin Films of Copper (II) Oxide and Copper (I) Oxide. *J. Appl. Phys.* **2001**, *90* (8), 4256−4264.
(67) Grosvenor, A. P.; Kobe, B. A.; Biesinger, M. C.; McIntyre, N. S. Investigation of Multiplet Splitting of Fe 2p XPS Spectra and Bonding in Iron Compounds. *Surf. Interface Anal.* **2004**, *36* (12), 1564−1574.
(68) Muir, A. H.; Wiedersich, H. An Investigation of $CuFeO_2$ by the Mössbauer Effect. *J. Phys. Chem. Solids* **1967**, *28* (1), 65−71.
(69) Galakhov, V. R.; Poteryaev, A. I.; Kurmaev, E. Z.; Anisimov, V. I.; Bartkowski, S.; Neumann, M.; Lu, Z. W.; Klein, B. M.; Zhao, T. R. Valence Band Spectra and Electronic Structure. *Phys. Rev. B: Condens. Matter Mater. Phys.* **1997**, *56* (8), 4584−4591.